ACS APPLIED MATERIALS & INTERFACES

www.acsami.org Research Article

Improving the Thermal Stability of Inverted Organic Solar Cells by Mitigating the Undesired MoO_3 Diffusion toward Cathodes with a High-Ionization Potential Interface Layer

Qian Xi, Jian Qin, Oskar J. Sandberg, Na Wu,* Rong Huang, Yifan Li, Maria Saladina, Carsten Deibel, Ronald Österbacka,* and Chang-Qi Ma*

Cite This: *ACS Appl. Mater. Interfaces* 2025, 17, 15456−15467 Read Online

ACCESS | Metrics & More | Article Recommendations | Supporting Information

ABSTRACT: Understanding the thermal degradation mechanism of organic solar cells (OSCs) and developing strategies to enhance their thermal stability are crucial before they can be commercialized. In this paper, we demonstrated that in a structure-inverted ITO/ZnO/PM6/L8-BO/TCTA/MoO_3/Ag solar cell, a thin 4,4′,4″-tris(carbazol-9-yl)-triphenylamine (TCTA) film between MoO_3 and PM6:L8-BO can significantly suppress the fast short circuit current (J_{SC}) loss and the slow but continuous open circuit voltage (V_{OC}) and fill factor (FF) decay upon 150 °C thermal annealing. XPS and TOF−SIMS results confirm that thermal annealing leads to the formation of $(MoO_3)^-$ at the MoO_3/PM6/L8-BO interface and the diffusion of $(MoO_3)^-$ through the photoactive layer. The diffused $(MoO_3)^-$ act as acceptor-type impurities that leads to *p*-doping of the photoactive layer, increasing charge recombination within the photoactive layer and reducing J_{SC}. In addition, the accumulation of $(MoO_3)^-$ at the cathode interface leads to *p*-doping at the cathode interface and consequently decreases V_{OC} and FF. The thermally induced interfacial degradation model is supported by detailed drift-diffusion simulations. The TCTA-interlayer minimizes the $(MoO_3)^-$ diffusion, thereby stabilizing the cell performance against thermal annealing. The TCTA-incorporating cells showed a high PCE of over 16% after high-temperature hot-press encapsulation, and the resulting cells showed excellent thermal stability under 85 °C.

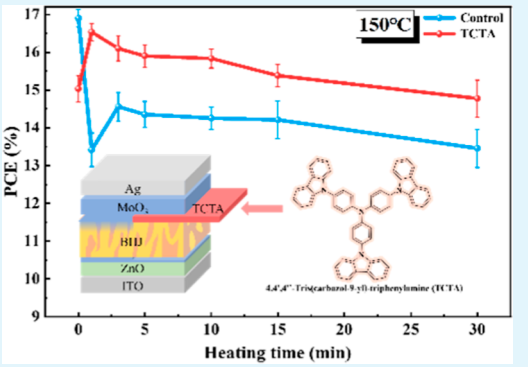

KEYWORDS: *organic solar cells, thermal stability, MoO_3 diffusion, interfacial modification, 4,4′,4″-tris(carbazol-9-yl)-triphenylamine*

1. INTRODUCTION

Organic solar cells (OSCs) have become the focus of scientific and industrial research due to their advantages of printing process compatibility,[1,2] intrinsic flexibility,[3−5] and good semitransparency.[6,7] The high extinction coefficient of non-fullerene acceptors (NFAs) increases the light absorption capability of the cells.[8] By mixing with wide band gap donors, a high power conversion efficiency (PCE) of over 20% was reported for the bulk heterojunction (BHJ) solar cells by reducing the undesired nonradiative open circuit voltage (V_{OC}) loss of the cells,[9] demonstrating a high possibility of commercialization of OSCs. However, the stability of OSCs remains a crucial obstacle to their industrial application.

Pathways that lead to the performance decay of OSCs can be divided into two categories: (i) extrinsic degradations, including weathering effects of the electrode,[10] and degradation of the BHJ[11,12] or the interface layers[13] by water and/or oxygen ingression, and (ii) intrinsic degradations, such as BHJ (nano)morphological changes[14−16] and increased interfacial defects[17−19] caused by light exposure,[20,21] electrical stress,[22] or thermal aging[23−25] In principle, water and oxygen ingression can be reduced by good encapsulation.[26,27]

Recently, photon-induced decomposition of NFA molecules at the ZnO interface was confirmed,[28,29] which can be reduced by passivating the surface defects of the ZnO layer,[30−32] demonstrating possible ways to solve the photostability issue of OSCs. In addition, thermal stress on BHJ solar cells is usually inevitable, such as during hot-press encapsulation or heat accumulation during operation, which could cause morphological changes in the BHJ. Using organic semiconductors with high glass transition temperature (T_g),[33,34] a combination of donor and acceptor with suitable miscibility,[35−37] and incorporating a third component into the active layer[38,39] are found to be helpful in improving the BHJ nanomorphology

Received: December 11, 2024
Revised: February 19, 2025
Accepted: February 25, 2025
Published: March 1, 2025

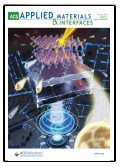

https://doi.org/10.1021/acsami.4c21773
ACS Appl. Mater. Interfaces 2025, 17, 15456−15467

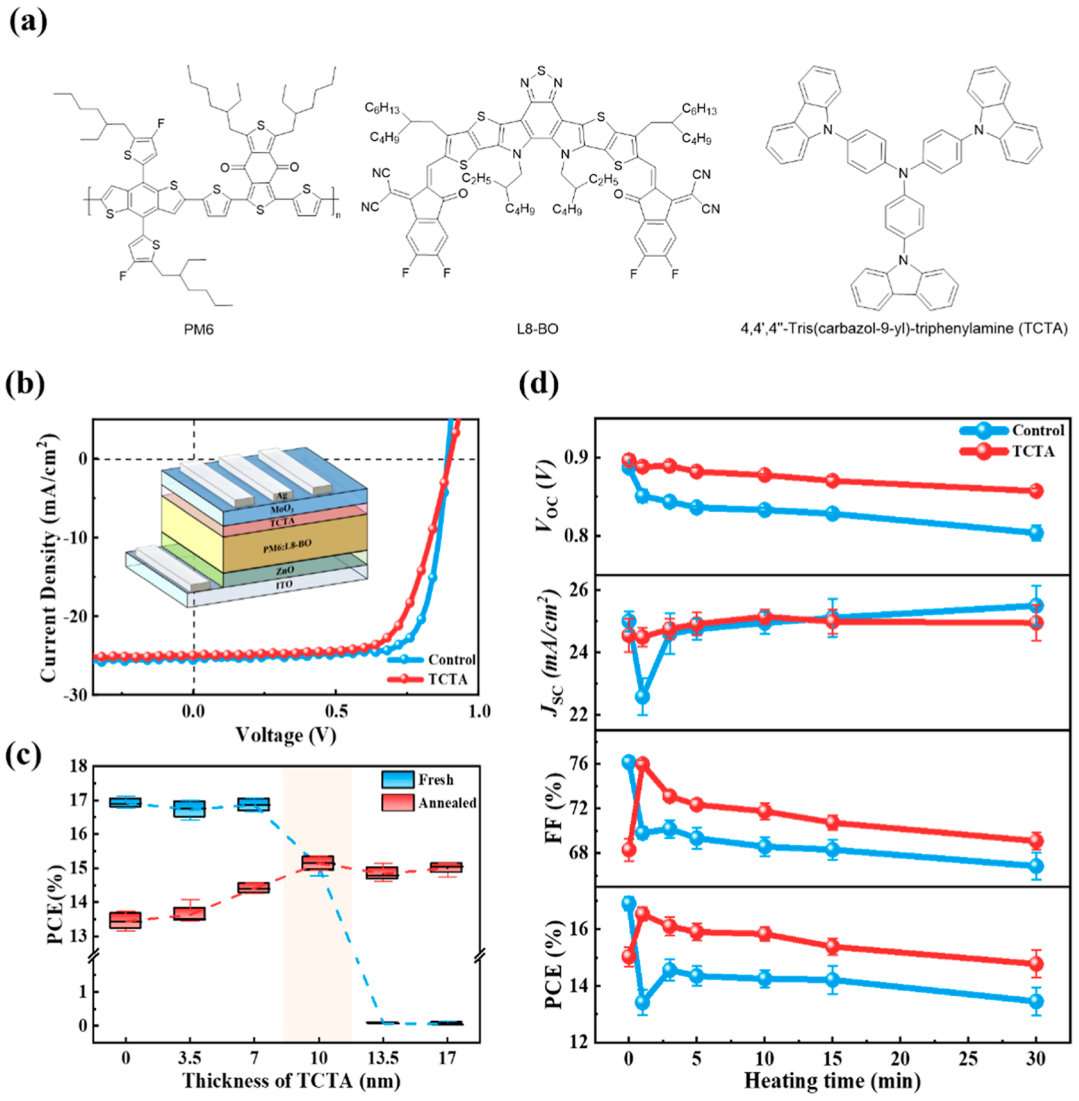

Figure 1. (a) Chemical structure of PM6, L8-BO, and TCTA; (b) illustration of the device structure and the representative $J-V$ curve of control device and TCTA device; (c) PCE of devices with different thicknesses of TCTA before and after annealing at 150 °C; and (d) thermal aging curve for V_{OC}, J_{SC}, FF, and PCE at 150 °C for 30 min.

and stability of the cells. In addition to the BHJ layer, the interfaces between the photoactive layer and the transport layer have also been found to be sensitive to thermal stress. For instance, Hu et al.[40] reported that the polyethylenimine (PEI) interfacial layer reacts more vigorously with the acceptor molecules when the cell is annealed at 160 °C, leading to a significant decrease in PCE. Our previous work has shown that the reaction of MoO_3 with the photoactive layer upon annealing also reduces the V_{OC} and fill factor (FF) and consequently also the PCE.[41] Our initial efforts found that a thin C_{60} layer (around 3 nm) does not affect the overall PCE but prevents the contact of MoO_3 with the active layer, thus effectively improving the device's thermal stability.[41]

In this study, 4,4′,4″-tris(carbazol-9-yl)-triphenylamine (TCTA) was introduced as an interfacial layer between MoO_3 and the photoactive layer through thermal evaporation in inverted OSCs. Our experimental results found that a thin TCTA layer (around 10 nm) can improve the efficiency of the cells after thermal annealing at 150 °C, retaining efficient charge extraction upon thermal annealing. Detailed experiments, including atomic force microscopy (AFM), X-ray photoelectron spectroscopy (XPS), and TOF−SIMS, demonstrated that TCTA can block the contact of the photoactive layer with thermally deposited MoO_3, as observed as a reduced formation of Mo^{5+}. Additionally, TCTA inhibits the diffusion of MoO_3 through the photoactive layer during annealing, which leads to a smaller decrease in the short circuit current (J_{SC}). We developed a model based on drift-diffusion simulations where p-doping of the photoactive layer by $(MoO_3)^-$ leads to a loss of J_{SC} during the initial stages of annealing, while at longer annealing times, the $(MoO_3)^-$ accumulates at a thin region close to the cathode interface, causing recombination and subsequent voltage loss. We demonstrated for the first time that the organic semiconductor TCTA as an interfacial barrier layer can effectively enhance the thermal stability of OSCs. Compared to atomic layer deposition and thermal evaporation of C_{60}, it provides a simple method and low-cost materials to enhance the thermal stability of OSCs.

https://doi.org/10.1021/acsami.4c21773
ACS Appl. Mater. Interfaces 2025, 17, 15456−15467

Table 1. Performance Parameters of the Inverted PM6/L8-BO Cells without or with the TCTA Layer (10 nm) upon Thermal Annealing at 150 °C for Different Times

interlayer	annealing time (min)	V_{OC} (V)[a]	J_{SC} (mA/cm^2)[a,b]	FF (%)[a]	PCE (%)[a]	PCE_{max} (%)[c]
control	0	0.888 ± 0.003	25.01 ± 0.32	76.15 ± 0.51	16.90 ± 0.23	17.28
	1	0.851 ± 0.008	22.59 ± 0.58	69.80 ± 0.52	13.42 ± 0.44	14.14
	3	0.844 ± 0.007	24.61 ± 0.65	70.16 ± 0.80	14.56 ± 0.38	15.31
	5	0.836 ± 0.002	24.75 ± 0.33	69.33 ± 0.97	14.35 ± 0.35	14.90
	10	0.833 ± 0.002	24.95 ± 0.36	68.57 ± 0.86	14.26 ± 0.30	14.68
	30	0.804 ± 0.010	25.50 ± 0.64	66.81 ± 1.19	13.45 ± 0.50	14.22
TCTA (10 nm)	0	0.898 ± 0.007	24.56 ± 0.54	68.28 ± 1.01	15.03 ± 0.34	15.46
	1	0.888 ± 0.005	24.50 ± 0.31	75.97 ± 0.34	16.54 ± 0.24	16.83
	3	0.890 ± 0.005	24.76 ± 0.34	73.10 ± 0.47	16.10 ± 0.33	16.59
	5	0.882 ± 0.005	24.92 ± 0.36	72.34 ± 0.50	15.90 ± 0.30	16.37
	10	0.878 ± 0.002	25.15 ± 0.24	71.74 ± 0.76	15.84 ± 0.25	16.14
	30	0.857 ± 0.004	24.96 ± 0.57	69.07 ± 0.74	14.78 ± 0.47	15.35

[a]: device performance data averaged from 8 individual cells. [b]: short circuit current measured under simulated AM 1.5G sunlight, which was calibrated with a certified Si cell. [c]: maximum PCE of the best cell.

2. RESULTS AND DISCUSSION

2.1. Photovoltaic Performance and Thermal Stability of the Cells. Figure 1a shows the chemical structures of PM6, L8-BO, and TCTA. Figure 1b shows the current density−voltage (J−V) curves of the champion inverted PM6/L8-BO solar cells with or without a TCTA layer in between the BHJ layer and MoO_3, where the device structure is shown as an inset in this figure. Figure S1 illustrates the energy bands of the functional layers of the cells. TCTA has a higher ionization energy (IE) of 5.83 eV than PM6 (5.43 eV), which is beneficial for forming a better ohmic contact at the anode with MoO_3.[42] The photovoltaic performance data of the control cells without a TCTA interlayer are listed in Table 1. The control cells showed an average PCE of 16.90%, with the highest PCE of 17.28%, comparable to that of the inverted PM6:L8-BO cells reported in the literature.[17,43] Solar cells with TCTA interlayers with thicknesses ranging from 3.5 to 17.0 nm were fabricated and tested. The photovoltaic performances of the 10 nm TCTA cells are listed in Table 1 for comparison and the comprehensive photovoltaic performance data of the cells are listed in Table S1. The correlation of the PCE of cells with different TCTA layer thicknesses is depicted in Figure 1c. As shown here, cells with a thin TCTA layer (3.5 and 7.0 nm) showed average PCEs of 16.53% and 16.86%, similar to the control cells, suggesting that a thin TCTA layer has a negligible impact on the device performance. When the TCTA layer thickness is increased to 10 nm, the device performance decreases to an average PCE of 15.03%, mainly due to the decrease in FF (Figure 1c and Table 1). Further increasing the TCTA layer thickness to 13.5 and 17.0 nm results in significant decreases of J_{SC} and FF, yielding a PCE of less than 0.1% (Table S1). This can be ascribed to the significantly decreased conductivity in thicker TCTA layer.

Our previous work demonstrated that when the annealing temperature is 150 °C, the degradation of cell performance is mainly caused by the MoO_3 interface.[41] To further investigate the effect of the interface on thermal stability, we tested the device performance of the cells under thermal annealing at 150 °C. The comprehensive evolution of the photovoltaic data of cells with different TCTA layer thicknesses is shown in Figure S2. Figure 1d depicts the evolution of the device performance of the TCTA-free (referred to as the control cell) and the cells with a 10 nm TCTA interlayer (the TCTA cell) under thermal annealing at 150 °C. Similar to our previous report, the control cells showed a continuous decrease in V_{OC} and FF with increased annealing time. However, the J_{SC} of the cells rapidly decreases after 1 min of thermal annealing but recovers after 3 min annealing and remains stable after that, resulting in a "check-mark" pattern under thermal annealing. The overall PCE showed a trend similar to that of J_{SC}, with a rapid decrease followed by a partial recovery during thermal annealing. Owing to the continuous V_{OC} and FF decrease, an overall ∼20% PCE decrease was found for the control cells (Table 1). In contrast, including a thin TCTA film significantly suppresses the decrease in J_{SC} during the first minute of annealing, yielding a much slower PCE decay (Figure S3).

Interestingly, although the cells with a 10 nm TCTA interlayer showed poor initial device performance, a significant improvement in the FF was found after annealing for 1 min at 150 °C, yielding the highest PCE of 16.83%, comparable to the initial value of the control cell. The TCTA-cells showed also more stable V_{OC} and FF, leading to better PCE stability compared to the control cells. The external quantum efficiency (EQE) spectra show that the control and the TCTA cells exhibit similar integrated J_{SC} values after annealing (Figure S4). Overall, the 10 nm TCTA-based cells showed a highest PCE of 16.14% and 15.38% after thermal annealing at 150 °C for 10 and 30 min, respectively, which is considerably higher than that of the control cell (14.68% and 14.22%). Notably, the cells with a thicker TCTA layer (13.5 and 17.0 nm) showed average PCEs of 14.84% and 14.74% after thermal annealing for 30 min (Figure 1c), demonstrating the excellent heat tolerance of the TCTA cells. These results suggest that the MoO_3/BHJ interface is responsible for the performance decay during thermal annealing and that a thin TCTA interlayer can mitigate the performance decay upon thermal annealing.[41]

To eliminate the impact of silver diffusion and reactions on the thermal stability, we then compared the influence of preannealing on the device performance of the ITO/ZnO/PM6/L8BO/MoO_3 and ITO/ZnO/PM6/L8BO/TCTA/MoO_3 films (Figure S5) prior to the completion of the cells. As seen here, after annealing at 150 °C for 1 min, the J_{SC} decreased from 24.83 to 20.45 mA/cm^2 and then increased to 21.90 mA/cm^2, which is consistent with the variation during annealing of the complete device. For the TCTA-cell, J_{SC} decreased slightly from 24.34 mA/cm^2 to 23.05 mA/cm^2 after 1 min annealing and then stable at 23.24 mA/cm^2. The results further corroborate that the interface changes of MoO_3 with

https://doi.org/10.1021/acsami.4c21773
ACS Appl. Mater. Interfaces 2025, 17, 15456−15467

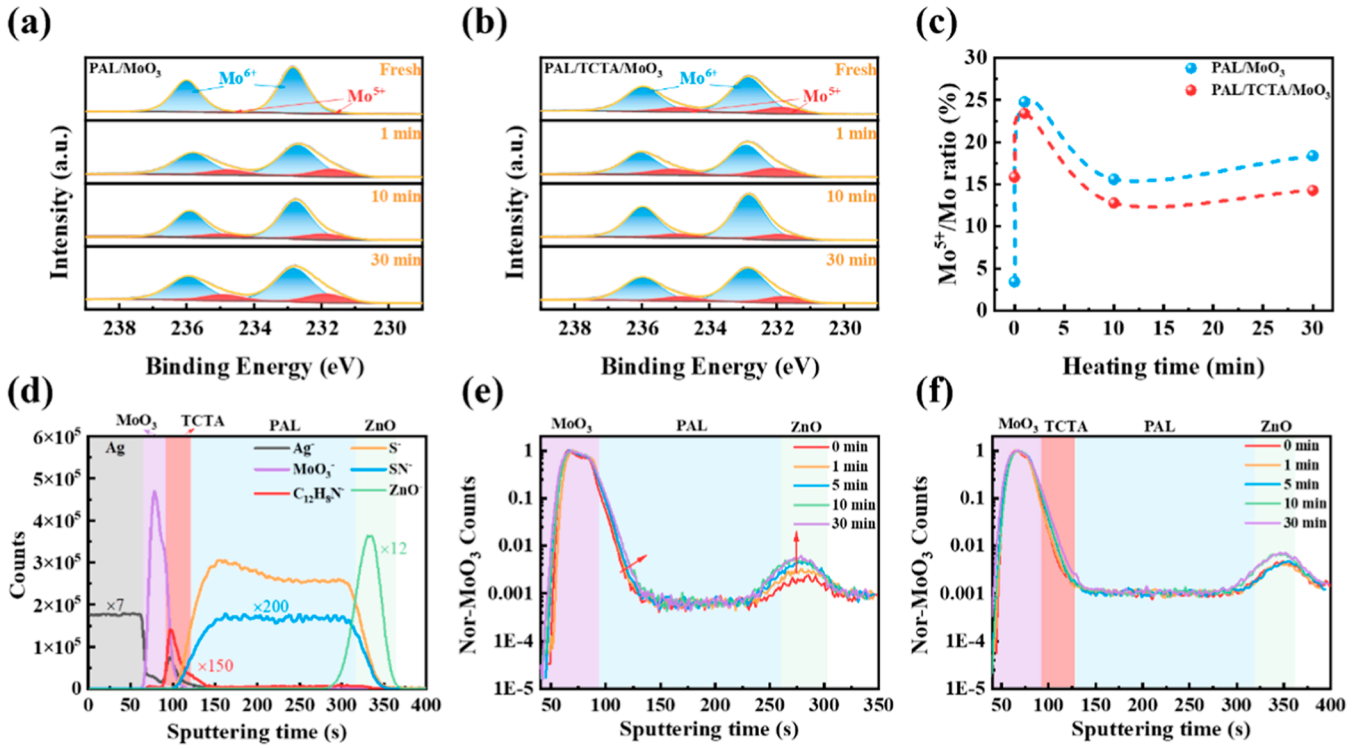

Figure 2. XPS spectra of Mo 3d for BHJ/MoO_3 (a) and BHJ/TCTA/MoO_3 (b) films annealed at different times; (c) evolution of Mo^{5+}/Mo contents of different films under thermal annealing. Representative TOF−SIMS depth profile of cells: negative ion depth profile of the fresh (d) TCTA-cells (note that due to some signal intensities being relatively low, the intensities of Ag^-, $C_{12}H_8N^-$, SN^-, and ZnO^- were multiplied by 7, 150, 200, and 20, respectively for a more intuitive comparison); and (e,f) MoO_3^- profile of the control (e) and TCTA (f) cells before and after annealing at 150 °C for different times (note that etching starts from the silver electrode).

the photoactive layer after annealing led to a rapid decline and recovery in the J_{SC}.

2.2. Surface Morphology Changes and the Diffusion of $(MoO_3)^-$. To better understand the interaction between MoO_3 with the photoactive layer and TCTA, the surface morphology and the chemical state of Mo atoms were investigated. Figure S6 shows the surface morphology of the PM6/L8-BO and PM6/L8-BO/TCTA (10 nm) films deposited on the ZnO surface before and after thermal annealing, respectively. It can be seen that the surface root mean surface roughness (R_q) of the PM6/L8-BO film increased from 1.04 to 1.99 nm after thermal annealing at 150 °C for 30 min, which is ascribed to the change of crystallite size and packing of donor and acceptor upon thermal annealing.[44] With 10 nm TCTA, the R_q of the PM6/L8-BO/TCTA film is decreased to 0.84 nm, indicating that TCTA could smooth the PM6/L8-BO surface. The lower roughness facilitates a more uniform deposition of MoO_3. Surprisingly, R_q decreased further to 0.31 nm after annealing, indicating that TCTA stabilizes the morphology of the active layer.

We then investigated the interactions of MoO_3 with PM6/L8-BO and TCTA layers by checking the Mo valence state at the interface. Figure 2a−b shows the measured Mo 3d XPS spectra at the MoO_3/PM6/L8-BO and MoO_3/TCTA interfaces at different annealing times. Two sets of peaks were measured, which can be fitted to Mo^{6+} (232.7 and 235.9 eV) and Mo^{5+} (231.7 and 234.8 eV).[45] The ratio of Mo^{5+} to overall Mo atoms was then estimated from the areas, and the evolution of Mo^{5+}/Mo ratios is shown in Figure 2c. All of these Mo^{5+}/Mo ratio points were connected via a smooth curve. As seen here, for the TCTA-free film, the Mo^{5+}/Mo ratio increases significantly from 3.5% to 24.8% after annealing for 1 min and then decreases slightly to 15.6% with the increase of annealing time. The increase of the Mo^{5+} ratio at first annealing minute indicates the reduction of MoO_3 to $(MoO_3)^-$ by the photoactive layer.[46] In contrast, for the fresh MoO_3/TCTA interface, a high Mo^{5+}/Mo ratio of 15.9% was measured, indicating a strong interaction of MoO_3 with TCTA during the deposition of MoO_3.[42] Like the MoO_3/BHJ film, the Mo^{5+}/Mo ratio of the MoO_3/TCTA interface increased to 23.4% after annealing for 1 min, indicating a continuous reduction of MoO_3 to $(MoO_3)^-$ at that interface. The Mo^{5+} content remains at 12.8% upon further thermal annealing, indicating a stabilized MoO_3/TCTA/BHJ interface.

The diffusion of MoO_3 into the active layer of BHJ solar cells has been suggested in the past.[47] Furthermore, Yin et al. reported that the diffusion of MoO_3 into the BHJ layer of P3HT/$PC_{61}BM$ cells depends on the thermal annealing process of the cells.[46] To better understand the impact of MoO_3 on device performance during thermal annealing and the role of TCTA in enhancing thermal stability in our case, TOF−SIMS was utilized to assess the distribution of different materials within the cells. Figures S7 and 2d show the representative fragment distribution profiles of the fresh control and TCTA cells. Given that SN^- and $C_{12}NH_8^-$ fragments exclusively originate from L8-BO and TCTA (Figure S8), the depth profile of these two fragments is then considered as the distribution of L8-BO and TCTA, respectively. Different functional layers were then identified by the distributions of the characterized ion fragments, as shown in Figure 2d. TCTA was successfully deposited on the

https://doi.org/10.1021/acsami.4c21773
ACS Appl. Mater. Interfaces 2025, 17, 15456−15467

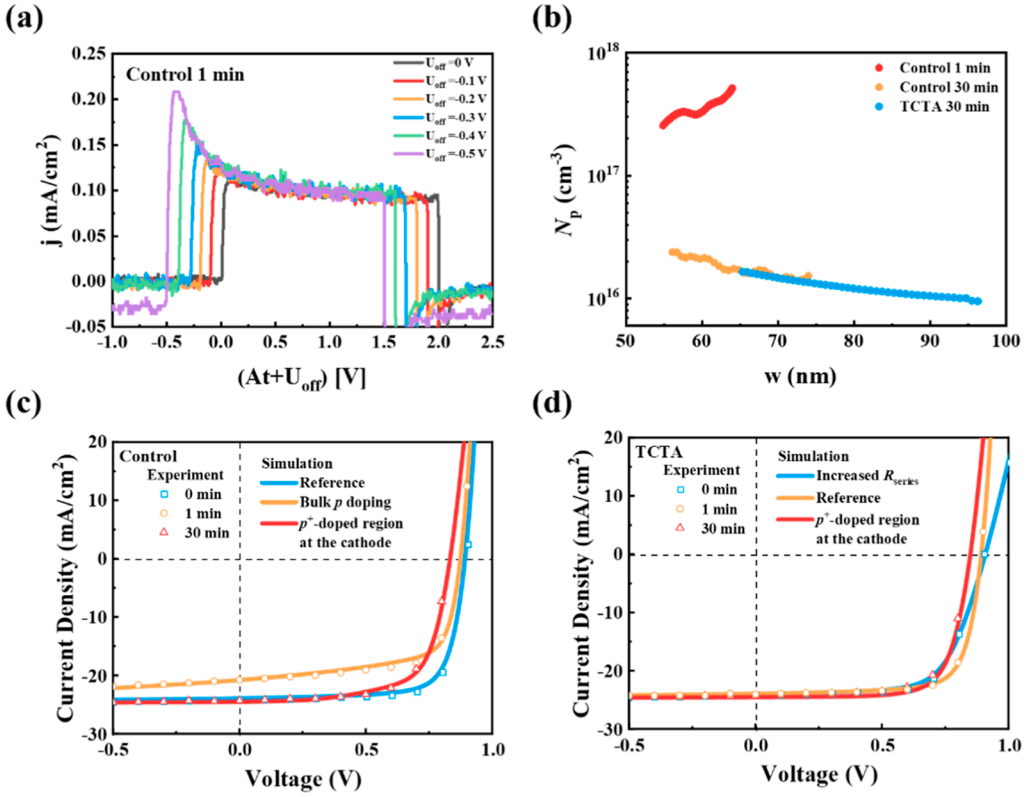

Figure 3. Experimental CELIV current transients: (a) control device annealed for 1 min plotted as a function of applied voltage ($At + U_{off}$) with the voltage rise speed A = 2 V/1 ms; (b) doping concentration at the distance (depletion width) w from the anode for control and TCTA devices after annealing; and experimental and simulated J−V curves: (c) control device and (d) TCTA device.

BHJ layer, separating the MoO_3 layer from the BHJ layer (Figure 2d).

Figure 2e,f illustrates the distribution of $(MoO_3)^-$ in control and TCTA-cells after annealing for different times. As seen here, besides a high intensity of the $(MoO_3)^-$ signal at the anode side, a small but clearly detectable signal of $(MoO_3)^-$ was also measured at the interface between the BHJ layer and ZnO even for the annealing-free cell, indicating that MoO_3 can diffuse through the BHJ layer even during the thermal deposition of MoO_3. For longer annealing times, an increased broadening of the $(MoO_3)^-$ distribution at the MoO_3/BHJ interface and a higher $(MoO_3)^-$ signal intensity at BHJ/ZnO was detected, suggesting the continuous diffusion of MoO_3 during thermal annealing. Similarly, diffusion of MoO_3 through the TCTA layer and broadening of the $(MoO_3)^-$ signal at the anode side were also measured for the TCTA-cell (Figure 2f). However, no increase of the $(MoO_3)^-$ signal was observed for the first 5 min of thermal annealing, suggesting that TCTA can slow down the diffusion of MoO_3 during the thermal annealing.

Interestingly, the diffusion of TCTA across the BHJ layer is also detected, as indicated by the progressive decrease and increase of the $C_{12}H_8N^-$ signal at the anode and cathode sides, respectively (Figure S9a). The diffusion of TCTA yielded high and balanced TCTA at both electrode interfaces and a relative high concentration within the BHJ layer. The penetration of TCTA through the photoactive layer results in the thinning of the TCTA layer at the interface, ultimately fostering an improved contact between the BHJ layer and MoO_3, as confirmed by the SN^- profile in the TOF−SIMS result (Figure S9b).

2.3. *p*-Doping of the Photoactive Layer. The increased levels of MoO_3 within the active layer can be directly correlated to the lowered device performance. To understand the role of MoO_3 on device performance upon thermal annealing, we conducted charge extraction by linearly increasing voltage (CELIV) measurements in the reverse bias at small voltage rise speed $A = U_{max}/t_{pulse}$ (U_{max} and t_{pulse} are the amplitude and duration of the reverse-biased voltage pulse, respectively, Figure S10a). Under these conditions, the corresponding CELIV current transients are capacitive and given by $j = CA$, where C is the capacitance of the active layer. We measured CELIV transients on control and TCTA devices before and after different annealing times (Figure S10). Before annealing, all devices show a flat CELIV transient response consistent with an undoped active layer.[48] However, the control device annealed at 1 min showed clear evidence of a bulk doping-induced capacitive current transient, as shown in Figure 3a. In this case, the current transient is determined by the depletion layer capacitance, with the associated bulk doping-induced depletion layer width w being voltage dependent.[48] This is seen as a dependence of the measured current transients on the applied time-dependent voltage $U(t) = At + U_{off}$, where U_{off} is the applied offset (dc) voltage.[48] After annealing for 30 min, the doping-induced capacitive current response is smaller, meaning that the capacitance is smaller, in agreement with a reduced doping concentration in the bulk (larger w) due to dopants accumulated at the cathode. On the contrary, the doping process is less pronounced in all cases for TCTA devices compared with control devices.

By plotting j^{-2} as a function of $U(t)$ (Figure S11), we can estimate the "average" doping level in the depletion region as

https://doi.org/10.1021/acsami.4c21773
ACS Appl. Mater. Interfaces 2025, 17, 15456−15467

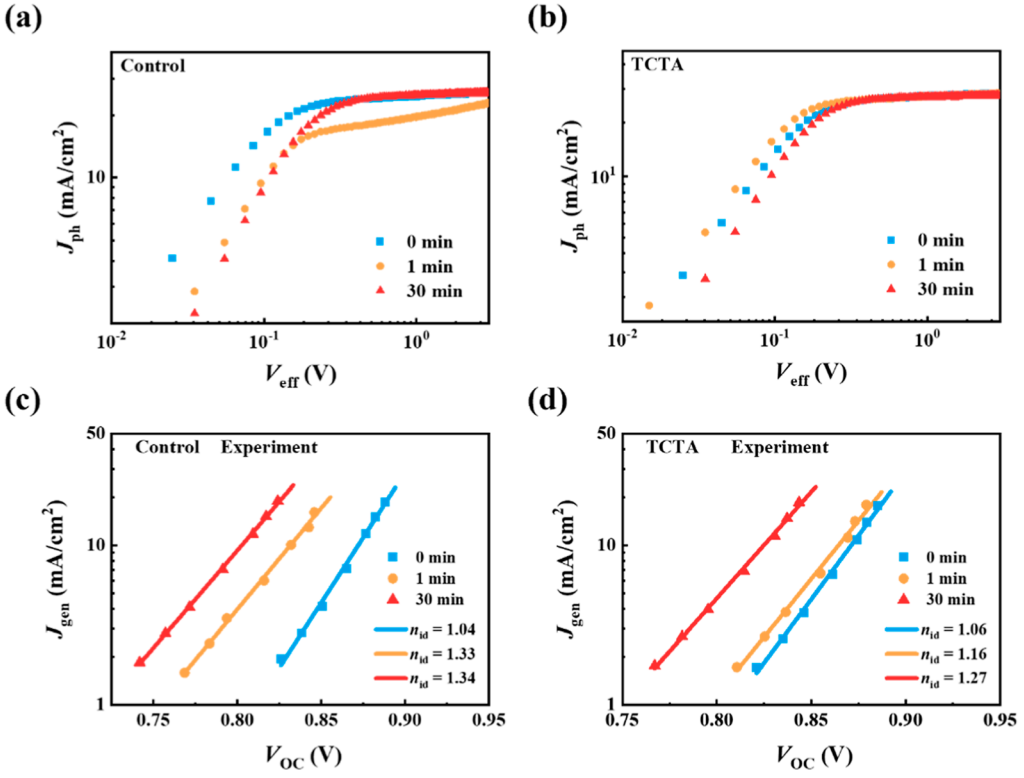

Figure 4. Photocurrent density versus effective voltage curves of the control (a) and TCTA-cells (b) upon different annealing times. Correlation of generated current density (j_{gen}) and open circuit voltage (V_{OC}) with changes of the recombination ideality factor n_{id} of the control (c) and TCTA-cells (d) obtained from experiment upon different annealing times.

$N_p = 1.3 \times 10^{17}$ cm^{-3} in the control device annealed for 1 min. However, the doping profile is expected to be quite nonuniform due to the diffusion during annealing. The doping profile with the anode distance can be extracted based on the measured voltage dependent (depletion layer) capacitances from CELIV.[49] In Figure 3b, we show the estimated doping concentration as a function of w, reflecting the distance from the anode, for the control and TCTA devices.[49] We note that only the 1 min annealed control device shows a doping concentration at least 10 times higher than all the other devices. However, it should be stressed that the extracted doping concentration for the 30 min annealed devices are likely below the detection limit of this method, and the corresponding N_p should thus be considered upper limit estimates.[50]

Numerical device simulations were performed for the cells. To this end, we used a drift-diffusion model, which accounts for both electrical effects (including charge transport, recombination, and space charge) as well as optical interference effects.[51] Because of its deep-lying conduction band, MoO_3 in its neutral state is generally expected to act as an acceptor-type impurity for organic layers. When present in the photoactive layer, MoO_3 can thus accept an electron from the HOMO level of PM6, resulting in the p-type doping of the BHJ layer. In this process, $(MoO_3)^-$ is formed as Mo^{6+} is reduced to Mo^{5+}. Additionally, MoO_3 may also act as a recombination center for photogenerated charge carriers within the BHJ. In the simulations, diffused MoO_3 in the photoactive layer is treated as a deep acceptor-type traps, of density N_t, being neutral when occupied by a hole and negatively charged (i.e., in the form $(MoO_3)^-$) when occupied by an electron. A MoO_3 state can be reduced to $(MoO_3)^-$ by capturing an electron from either the donor HOMO or acceptor LUMO level, resulting in p-type doping and electron trapping, respectively. Conversely, $(MoO_3)^-$ can be oxidized back to MoO_3 either through recombination with a free hole from the donor HOMO or by thermal release of a free electron to the acceptor LUMO (a similar dedoping in P3HT films by annealing has been reported[52]). Further details of the device model are given in the Methods section.

Figure 3c shows the experimental and simulated $J-V$ curves of the control cells. The fresh control cell (before thermal annealing, i.e., the 0 min case) is assumed to be trap-free and undoped, corresponding to a negligible MoO_3 content in the active layer. We note that including a narrow region with a high density of MoO_3 impurities near the anode contact yielded a curve very similar to the reference cell. Instead, the J_{SC} decrease of the 1 min case could be reproduced by assuming $N_t = 1.7 \times 10^{17}$ cm^{-3} throughout the entire BHJ layer. The results N_t obtained from simulation based on the experimental $J-V$ curve are close to the value of N_p (1.3×10^{17} cm^{-3}) measured by CELIV. Figure S12 shows that increasing the doping concentration generally gives rise to an enhanced photocurrent loss. However, for N_t below 3×10^{16} cm^{-3}, the effect of bulk doping becomes negligible in these devices, with the $J-V$ curve being indistinguishable from the undoped case. The decrease in J_{SC} is attributed to increased recombination due to the formation of a doping-induced space charge region and trap-assisted recombination in the bulk.[53−55] On the other hand, the 30 min case with recovered J_{SC} and reduced V_{OC} can be reproduced by assuming that MoO_3 is instead accumulated at the cathode. In Figure 3c, this is modeled by assuming $N_t = 6 \times 10^{18}$ cm^{-3} within the first 5 nm from the ZnO/BHJ contact, while $N_t = 0$ for the remainder of the active layer. The

https://doi.org/10.1021/acsami.4c21773
ACS Appl. Mater. Interfaces 2025, 17, 15456−15467

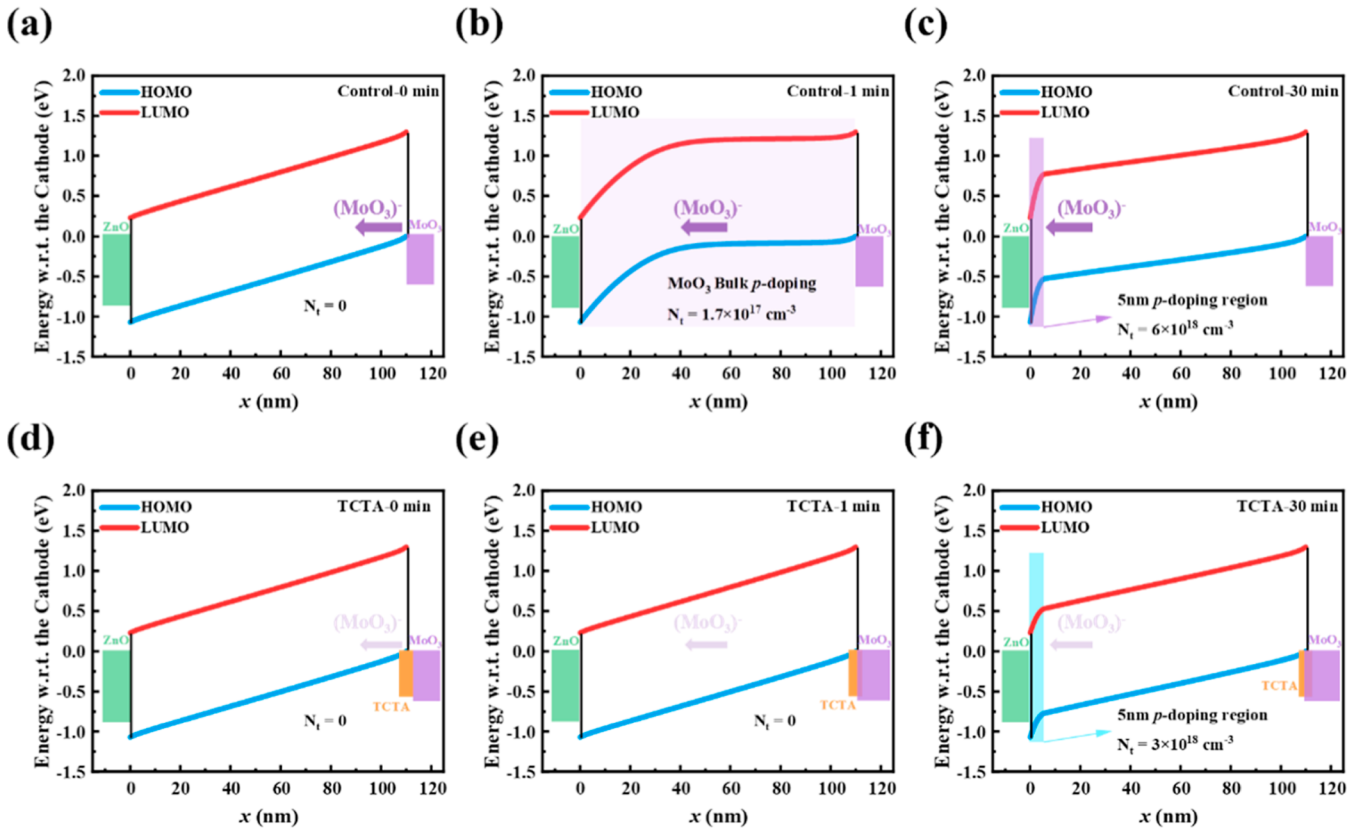

Figure 5. Proposed mechanism for stability improvement of the cells by the TCTA layer: energy band bending of the control annealing for (a) 0 min, (b) 1 min, and (c) 30 min and TCTA-cells annealing for (d) 0 min, (e) 1 min, and (f) 30 min.

reduction in the V_{OC} is primarily attributed to the high space charge density of ionized *p*-dopants $(MoO_3)^-$ at the cathode causing upward energy level bending, effectively increasing the injection barrier at this contact. These findings suggest that for devices without TCTA, MoO_3 diffuse into the active layer, initially causing bulk *p*-doping and subsequent J_{SC} loss. Eventually, during continuous thermal annealing, the bulk doping is reduced and instead concentrated at the cathode interface, seen as a continuous decrease in V_{OC} during the annealing process.

Figure 3d shows the experimental and simulated $J-V$ curves of the TCTA cells. We note that the limited hole extraction of fresh TCTA is particularly detrimental in devices with thicker TCTA layers, where severe S shapes are obtained. During thermal annealing, the TCTA layer inhibits diffusion of *p*-dopant ions into the active layer. Instead, *p*-dopant ions diffuse into the TCTA layer, resulting in a drastically increased conductivity in TCTA. As a result, the PCE of the TCTA device initially recovers after annealing, becoming similar to the PCE of the reference control device. The V_{OC} loss at longer times is again attributed to the accumulation of diffused *p*-dopant ions at the cathode. However, since the diffusion of MoO_3 is significantly reduced by TCTA, both the build-up in the bulk and the subsequent accumulation at the cathode contact are considerably smaller, resulting in an almost unnoticeable J_{SC} loss and smaller V_{OC} loss, respectively.

2.4. Influence of Thermal Annealing on Charge Extraction and Recombination. To substantiate the suggested mechanism and fully understand the effect of thermal annealing on the changes of J_{SC}, V_{OC}, and FF, further electrical measurements to probe the charge extraction and recombination of the cells were conducted. Figure 4a,b shows the plots of J_{ph} (photocurrent density) versus V_{eff} (effective voltage) for the control and TCTA-cells annealed at different times, respectively, where J_{ph} is the net photon generated current and V_{eff} is the effective voltage, defined as the difference between the applied voltage and V_0, where V_0 is the voltage when J_{ph} is zero. The ratio of the photocurrent density at short-circuit current and saturated photocurrent is used to estimate the charge collection efficiency (P_{coll}).[56,57] (Note that V_0 is not an exact point where the internal field is zero and photogeneration is zero because of photoshunt, but the photocurrent density versus effective voltage curves clearly show the field-dependent collection efficiency in the devices.) As shown, the $J_{ph}-V_{eff}$ line of the control device is flat when the V_{eff} exceeds 2 V for the initial cell, becomes sloped after annealing for 1 min, and then becomes flat again after a long annealing time. In contrast, the line of the TCTA-cell remains consistently flat, independent of the thermal annealing duration. These results indicate that initial 1 min thermal annealing of the control cell leads to a drastic decrease of the extraction rates, depending strongly on the applied electric field, consistent with doping-induced space charge build-up and enhanced trap-assisted recombination in the active layer.[53] The addition of the TCTA protection layer can mitigate this effect and, thus, stabilize the charge extraction.

We then used the Suns-V_{OC} method to further investigate the prevailing charge carrier recombination mechanism within the cells during different thermal annealing times.[58] Figure S13 in Supporting Information shows the $J-V$ curves of the cells before and after thermal annealing. The V_{OC} is related to j_{gen} via

https://doi.org/10.1021/acsami.4c21773
ACS Appl. Mater. Interfaces 2025, 17, 15456−15467

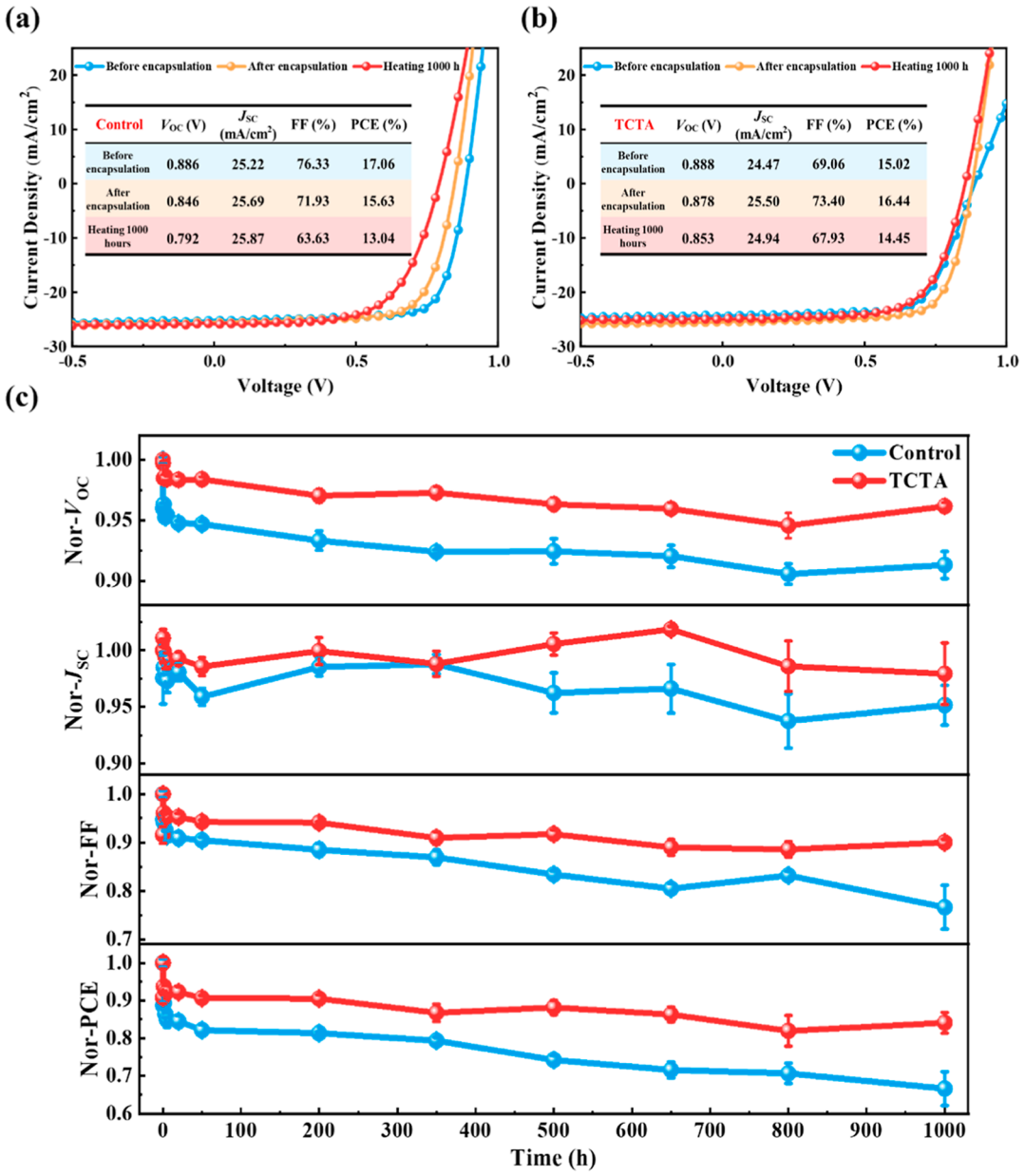

Figure 6. Current density−voltage (J−V) curves of the control (a) and TCTA-cells (b) before and after encapsulation and the following long-term thermal annealing. (c) Performance evolution of the cells upon 85 °C annealing over 1000 h.

$$j_{gen} = j_0 \exp^{(eV_{OC}/n_{id}kT)} \quad (1)$$

where n_{id} is the recombination ideality factor and j_0 the associated dark saturation current density. When plotting V_{OC} and j_{gen} as a function of V_{OC} and j_{gen} on a log-lin scale, a linear relationship in accordance with eq 1 is obtained as shown in Figure 4, where j_{gen} is estimated from the current density at −1 V. The corresponding n_{id} of the cells are indicated in Figure 4c. As shown, the n_{id} of the TCTA-free control cell increased from 1.03 to 1.33 after thermal annealing for 1 min. This result unambiguously indicates an increased trap-assisted recombination for the control cell after thermal annealing. With a further increase in the annealing time, n_{id} does not change significantly, indicating a balanced state of the cells. In contrast, the TCTA-cell shows a smaller increase in n_{id} after thermal annealing for 1 min compared to the control cell. After this, n_{id} is increased gradually until similar values to the TCTA-free cells. This confirms that the TCTA layer can reduce and delay the enhanced trap-assisted recombination (induced by diffused MoO_3) due to thermal annealing.

2.5. Discussion on the Thermal Stability of the Cells.

Combining the device physics and chemical changes of the cells upon thermal annealing, a thermal-induced degradation mechanism of the inverted polymer solar cells is proposed as follows (Figure 5). After the deposition of MoO_3 on the top of the polymer photoactive layer, most of the Mo atoms are in the form of Mo^{6+} and mainly located at the MoO_3/PAL interface (Figure 5a). 1 min thermal annealing generates Mo^{5+} in the form of $(MoO_3)^-$, which distributes over the photoactive layer leading to p-doping of the BHJ layer (Figure 5b). Such a bulk p-doping leads to significant J_{SC} decay, as shown in Figure 1d. $(MoO_3)^-$ further diffuses through the PAL and accumulates at the ZnO surface (Figure 5c), causing a high concentration region of negative space charge at the ZnO/PAL interface that

https://doi.org/10.1021/acsami.4c21773
ACS Appl. Mater. Interfaces 2025, 17, 15456−15467

leads to energy level bending and charge recombination in the thin interfacial region near the cathode contact with consequent loss of V_{OC} and FF as a result.

The TCTA interlayer reacts with MoO_3 already during the deposition of MoO_3, which yields a certain amount of Mo^{5+}. A 10 nm TCTA layer blocks the contact of MoO_3 with PAL and causes an increased series resistance leading to the lower FF (Figure 5d). By annealing the film, MoO_3 diffuses further into the TCTA film, doping the TCTA resulting in higher hole conductivity and improved hole extraction at the MoO_3/PAL interface (Figure 5e). The blocking effect of the TCTA layer inhibits the diffusion of MoO_3 into the photoactive layer, thus mitigating *p*-doping in the bulk. We note that TCTA might also form a charge−transfer complex with MoO_3 that may assist in reducing the *p*-doping of the photoactive layer. The combined effect is that a decrease in J_{SC} is not occurring. However, the MoO_3 accumulating at the cathode interface will still cause an increased energy level bending at the ZnO interface. Nevertheless, the concentration of negatively charged MoO_3 is lower than in the reference cells (Figure 5f), which consequently lowers the losses in V_{OC} and FF of the cells.

2.6. Highly Thermal Stable OCs with over 16% Efficiency after Encapsulation. Knowing that a thin TCTA layer can minimize the undesired performance loss upon high-temperature thermal annealing, we then tested the heat tolerance of the OSCs during hot-press encapsulation and long-term thermal annealing. PM6/L8-BO-based cells with or without TCTA protection layer were fabricated and encapsulated through a hot-pressing process at 120 °C for 5 min. The *J*−*V* curves of the control and TCTA cells before and after encapsulation are shown in Figure 6a,b. As seen here, the control cell exhibited significant PCE loss from 17.06% to 15.63% after encapsulation, while the TCTA cell showed a PCE enhancement from 15.02% to 16.44%, mainly owing to the recovery in FF. We tested the long-term thermal stability of devices after encapsulation at 85 °C. As shown in Figure 6c, the introduction of the TCTA protection layer significantly improved the long-term stability of the cells. The TCTA-cells retained 88% of their initial PCE after 1000 h annealing at 85 °C, whereas the control cells retained only 70%. The improvement in thermal stability mainly comes from the slowdown of the V_{OC} and FF decay. Overall, the incorporation of TCTA proved to be an effective method for enhancing the thermal stability of OSCs in practical applications.

3. CONCLUSIONS

In summary, through a systematic investigation of the chemical information on the anode interface, the diffusion of Mo atoms, and the device physics of inverted PM6/L8-BO cells upon 150 °C thermal annealing, we have verified that thermal annealing leads to the formation of Mo^{5+} in the form of $(MoO_3)^-$ at the MoO_3/PAL interface, acting as an acceptor-type impurity causing *p*-doping of the photoactive layer as well as a trapping center for photogenerated holes, leading to increased recombination. The MoO_3 diffuses into the PM6/L8-BO blend layer at already very short annealing times, consequently resulting in a notable decline in J_{SC} of the cell. At longer annealing times, MoO_3 diffusion leads to an accumulation of the $(MoO_3)^-$ at the ZnO cathode, leading to an effectively increased injection barrier due to band-bending with lowering of the FF and V_{OC} as a result. A thin layer of TCTA serves as an effective interfacial layer to block the direct contact of MoO_3 with PAL, which lowers the diffusion of MoO_3, and consequently enhances the thermal stability of the cells. The TCTA-containing cell showed over 16% PCE after hot-press encapsulation and retained 88% of initial PCE after 1000 h annealing at 85 °C, whereas the control cells retained only 70%.

4. METHODS

4.1. Device Fabrication, *J*−*V* Measurement, and Thermal Aging. The ITO substrates were customized on glass with a strip width of 3 mm. The ITO substrates were sequentially immersed in detergent aqueous solution, deionized water (twice), and ethanol (twice), each subjected to ultrasonic cleaning for 30 min. The cleaned ITO substrates were dried with dry and clean N_2 and treated with the O_2-plasma. After cooling to room temperature, a sol−gel ZnO solution prepared by dissolving 1:1 molar ratio of ethanolamine (ADAMAS-BETA Inc.) and zinc acetate dihydrate (Shanghai Titan Scientific Co., Ltd.) in 2-methoxyethanol (J&K Scientific) at a concentration of 0.45 mol/L was spin-coated onto the cleaned ITO glasses, with a spin speed of 2000 rpm, an acceleration of 3000 rpm/s, and a duration of 30 s. After spin-coating, the devices were annealed at 200 °C for 30 min. Subsequently, the devices were transferred to a N_2 glovebox, where PM6 (Organtec Ltd.) and L8-BO (Hyper Inc.) were weighed in a mass ratio 1:1.2 and added to a $CHCl_3$ (ADAMAS-BETA Inc.) solution containing 50% by weight of 1,4-dibromobenzene (DIB) purchased from TCI, with a PM6 concentration of 7.2 mg/mL. The mixed solution was stirred at 55 °C for 2 h and cooled to room temperature to obtain the active layer solution. 20 μL of the above active layer solution was spin-coated at a speed of 2000 rpm for 30 s. The devices were annealed at 85 °C for 5 min. After being annealed and cooled to room temperature, the device was transferred to a vacuum deposition chamber for the deposition of 15 nm MoO_3 and 100 nm Ag. TCTA devices were prepared by thermal evaporating 10 nm of TCTA (ADAMAS-BETA Inc.) onto the surface of the active layer thin film after annealing, with subsequent steps remaining unchanged.

The *J*−*V* curves of devices were measured using a digital source (Keithley 2400) under irradiation from an AM 1.5G solar simulator (model XES-40S3, power 100 mW/cm^2). The *J*−*V* curves and physical parameters such as V_{OC}, J_{SC}, FF, and PCE of the devices were synchronously recorded by using computer software. The effective photovoltaic area for each device was 0.09 cm^2.

4.1.1. Thermal Stability Testing. The devices were annealed on a hot plate inside a glovebox at a specified temperature and duration. Afterward, they were removed and allowed to cool to room temperature, and then the device efficiency was measured.

4.1.2. Hot Press Encapsulation. The cells were hot-press laminated a glass cover by commercially available polyolefin (POE) film using a hot-press machine (HP-Lab-10, Suzhou D&R Instruments). The process temperature and time were adjusted manually to get the optimized encapsulation condition, which is finalized to be 120 °C for 5 min.

4.2. CELIV Measurements. CELIV measurements were carried out with a home-built setup using a function generator (Agilent 33250A) and oscilloscope (RIGOL DS1104). The applied ramp-up voltage pulse was produced under a given offset voltage by the function generator, while the oscilloscope can measure the output voltage induced across its internal 50 Ω load resistor, allowing for the current to be obtained. An external resistor was added to the circuit to change the load resistance for improved signal detection. For the measurements, the ramp-up voltage pulse and the offset voltage were applied in reverse bias of the device, and the corresponding transient (reverse) current response was collected.

4.3. Numerical Device Simulation. For the device simulations, a drift-diffusion model is used. The model numerically solves the Poisson equation and the continuity equations for electrons and holes in the photoactive layer. Herein, the active BHJ layer is considered as an effective semiconductor, where the HOMO level of the donor and LUMO level of the acceptor correspond to the effective valence and conduction bands, respectively. An effective energy-level gap of 1.3 eV

https://doi.org/10.1021/acsami.4c21773
ACS Appl. Mater. Interfaces 2025, 17, 15456−15467

and effective densities of states of 10^{20} cm^{-3} are assumed. Furthermore, an injection barrier of 0.13 eV for electrons at the cathode and 0.1 eV for holes at the anode is used. The charge transport of electrons and holes is described by the drift-diffusion relations, while the recombination is composed of both bimolecular recombination between free electrons and holes and trap-assisted recombination via deep trap states within the gap. In this work, balanced carrier mobilities given by 5×10^{-4} $cm^2/(V\ s)$ and a Langevin reduction factor of 0.0025 for bimolecular recombination are assumed. The generation of charge carriers in the active layer is calculated using an optical transfer-matrix model, which accounts for the absorption, reflection, and interference effects between the different layers within the device stack.

4.4. XPS, AFM, and TOF-SIMS Measurements. *4.4.1. XPS Measurement.* After preparation of the active layer and TCTA, MoO_3 (6 nm) was deposited onto the surface. XPS spectra were measured using an ESCALAB 250Xi$^+$ spectrometer with a monochromatic Al−Kα X-ray source, using the C−C bonding component of amorphous carbon as a reference.

4.4.2. AFM Measurement. The active layer solution was spin-coated onto the ZnO surface on the ITO glass and annealed on a hot plate at 85 °C for 5 min, followed by the deposition of TCTA (10 nm). Subsequently, the surface roughness of the sample was analyzed at room temperature using a probe-based Park XE-120 atomic force microscope.

4.4.3. Matrix-Assisted Laser Desorption/Ionization Time-of-Flight Mass Spectrometry Measurement. To prepare complete devices with layer thickness consistent with control devices, various elements including Ag, Mo, O, S, SN, and Zn were detected for their distribution by in situ annealing at 150 °C in a high vacuum chamber, using an anion mode. The SIMS data were tested through a TOF-SIMS 5−100.

■ ASSOCIATED CONTENT

Supporting Information

The Supporting Information is available free of charge at https://pubs.acs.org/doi/10.1021/acsami.4c21773.

Performance parameters of cells with or without TCTA, schematic energy level arrangement of materials, $J-V$ curve and thermal aging curve for different thicknesses of TCTA devices, EQE spectra for control and TCTA devices before and after annealing, $J-V$ curves of different preannealing times after evaporation of MoO_3, AFM height images of the BHJ and BHJ/TCTA surface before and after annealing, TOF-SIMS negative ion depth profile of the fresh control cells, SIMS mass spectra of PM6, L8-BO, and TCTA, $C_{12}H_8N^-$ and SN^- TOF-SIMS depth profile within the TCTA-cell after annealing, a linearly increasing voltage pulse applied in CELIV, experimental CELIV current transients plotting the j and j^{-2} as a function of $(At + U_{off})$, simulated $J-V$ curves of varying bulk doping concentration, and $J-V$ curves under different light intensities for control and TCTA device at different annealing times (PDF)

■ AUTHOR INFORMATION

Corresponding Authors

Na Wu − *i-Lab & Printable Electronics Research Center, Suzhou Institute of Nano-Tech and Nano-Bionics, Chinese Academy of Sciences, Suzhou 215123, P. R. China;* Email: nwu2022@sinano.ac.cn

Ronald Österbacka − *i-Lab & Printable Electronics Research Center, Suzhou Institute of Nano-Tech and Nano-Bionics, Chinese Academy of Sciences, Suzhou 215123, P. R. China; Physics and Center for Functional Materials, Faculty of Science and Technology, Åbo Akademi University, Turku 20500, Finland;* orcid.org/0000-0003-0656-2592; Email: ronald.osterbacka@abo.fi

Chang-Qi Ma − *School of Nano-Tech and Nano-Bionics, University of Science and Technology of China, Baohe District, Hefei 230026, P. R. China; i-Lab & Printable Electronics Research Center, Suzhou Institute of Nano-Tech and Nano-Bionics, Chinese Academy of Sciences, Suzhou 215123, P. R. China;* orcid.org/0000-0002-9293-5027; Email: cqma2011@sinano.ac.cn

Authors

Qian Xi − *School of Nano-Tech and Nano-Bionics, University of Science and Technology of China, Baohe District, Hefei 230026, P. R. China; i-Lab & Printable Electronics Research Center, Suzhou Institute of Nano-Tech and Nano-Bionics, Chinese Academy of Sciences, Suzhou 215123, P. R. China*

Jian Qin − *School of Nano-Tech and Nano-Bionics, University of Science and Technology of China, Baohe District, Hefei 230026, P. R. China; i-Lab & Printable Electronics Research Center, Suzhou Institute of Nano-Tech and Nano-Bionics, Chinese Academy of Sciences, Suzhou 215123, P. R. China*

Oskar J. Sandberg − *Physics and Center for Functional Materials, Faculty of Science and Technology, Åbo Akademi University, Turku 20500, Finland*

Rong Huang − *Vacuum Interconnected Nanotech Workstation, Suzhou Institute of Nano-Tech and Nano-Bionics, Chinese Academy of Sciences (CAS), Suzhou 215123, P. R. China*

Yifan Li − *Vacuum Interconnected Nanotech Workstation, Suzhou Institute of Nano-Tech and Nano-Bionics, Chinese Academy of Sciences (CAS), Suzhou 215123, P. R. China;* orcid.org/0000-0002-3249-1778

Maria Saladina − *Institut für Physik, Technische Universität Chemnitz, Chemnitz 09126, Germany*

Carsten Deibel − *Institut für Physik, Technische Universität Chemnitz, Chemnitz 09126, Germany;* orcid.org/0000-0002-3061-7234

Complete contact information is available at: https://pubs.acs.org/10.1021/acsami.4c21773

Notes

The authors declare no competing financial interest.

■ ACKNOWLEDGMENTS

The authors would like to acknowledge the financial support from the National Natural Science Foundation of China (22075315) and the Suzhou Science and Technology Bureau (Grant No. SWY2022004). Research Council of Finland is acknowledged through project #357196 (O.J.S.) and project # 359833 (R.Ö.). M.S. and C.D. thank the Deutsche Forschungsgemeinschaft (DFG) for funding this work (Research Unit FOR 5387 POPULAR, Project No. 461909888). The authors are grateful for the technical support for Nano-X from Suzhou Institute of Nano-Tech and Nano-Bionics, Chinese Academy of Sciences.

■ REFERENCES

(1) Zheng, X. J.; Zuo, L. J.; Zhao, F.; Li, Y. K.; Chen, T. Y.; Shan, S. Q.; Yan, K. R.; Pan, Y. W.; Xu, B. W.; Li, C. Z.; Shi, M. M.; Hou, J. H.; Chen, H. Z. High-Efficiency ITO-Free Organic Photovoltaics with

Superior Flexibility and Upscalability. *Adv. Mater.* **2022**, *34* (17), 2200044.
(2) Wachsmuth, J.; Distler, A.; Liu, C.; Heumüller, T.; Liu, Y.; Aitchison, C. M.; Hauser, A.; Rossier, M.; Robitaille, A.; Llobel, M. A.; Morin, P. O.; Thepaut, A.; Arrive, C.; McCulloch, I.; Zhou, Y. H.; Brabec, C. J.; Egelhaaf, H. J. Fully Printed and Industrially Scalable Semitransparent Organic Photovoltaic Modules: Navigating through Material and Processing Constraints. *Sol. RRL* **2023**, *7* (21), 2300602.
(3) Wang, J. X.; Han, C. Y.; Han, J. H.; Bi, F. Z.; Sun, X. K.; Wen, S. G.; Yang, C. P.; Yang, C. M.; Bao, X. C.; Chu, J. H. Synergetic Strategy for Highly Efficient and Super Flexible Thick-film Organic Solar Cells. *Adv. Energy Mater.* **2022**, *12* (31), 2201614.
(4) Wang, S. H.; Peng, L.; Sun, H. B.; Huang, W. The future of solution processing toward organic semiconductor devices: a substrate and integration perspective. *J. Mater. Chem. C* **2022**, *10* (35), 12468−12486.
(5) Xu, Z.; Xu, G.; Luo, Q.; Han, Y.; Tang, Y.; Miao, Y.; Li, Y.; Qin, J.; Guo, J.; Zha, W.; Gong, C.; Lu, K.; Zhang, J.; Wei, Z.; Cai, R.; Yang, Y.; Li, Z.; Ma, C.-Q. In situ performance and stability tests of large-area flexible polymer solar cells in the 35-km stratospheric environment. *Natl. Sci. Rev.* **2023**, *10* (4), nwac285.
(6) Li, Y. X.; Huang, X. J.; Sheriff, H. K. M.; Forrest, S. R. Semitransparent organic photovoltaics for building-integrated photovoltaic applications. *Nat. Rev. Mater.* **2023**, *8* (3), 186−201.
(7) Liu, X.; Zhong, Z. P.; Zhu, R. H.; Yu, J. S.; Li, G. Aperiodic band-pass electrode enables record-performance transparent organic photovoltaics. *Joule* **2022**, *6* (8), 1918−1930.
(8) Gao, W.; Lin, F. R.; Jen, A. K. Y. Near-Infrared Absorbing Nonfullerene Acceptors for Organic Solar Cells. *Sol. RRL* **2022**, *6* (1), 2100868.
(9) Jiang, Y.; Sun, S.; Xu, R.; Liu, F.; Miao, X.; Ran, G.; Liu, K.; Yi, Y.; Zhang, W.; Zhu, X. Non-fullerene acceptor with asymmetric structure and phenyl-substituted alkyl side chain for 20.2% efficiency organic solar cells. *Nat. Energy* **2024**, *9*, 975−986.
(10) Han, Y. F.; Hu, Z. S.; Zha, W. S.; Chen, X. L.; Yin, L.; Guo, J. B.; Li, Z. Y.; Luo, Q.; Su, W. M.; Ma, C. Q. 12.42% Monolithic 25.42 cm^2 Flexible Organic Solar Cells Enabled by an Amorphous ITO-Modified Metal Grid Electrode. *Adv. Mater.* **2022**, *34* (17), 2110276.
(11) van der Pol, T. P. A.; van Gorkom, B. T.; van Geel, W. F. M.; Littmann, J.; Wienk, M. M.; Janssen, R. A. J. Origin, Nature, and Location of Defects in PM6:Y6 Organic Solar Cells. *Adv. Energy Mater.* **2023**, *13* (12), 2300003.
(12) Kim, D. H.; Wibowo, F. T. A.; Lee, D.; Krishna, N. V.; Park, S.; Cho, S.; Jang, S.-Y. Non-Fullerene-Based Inverted Organic Photovoltaic Device with Long-Term Stability. *Energy Environ. Mater.* **2023**, *6* (3), No. e12381.
(13) Lin, C.-T.; Hsieh, C.-T.; Macdonald, T. J.; Chang, J.-F.; Lin, P.-C.; Cha, H.; Steier, L.; Wadsworth, A.; McCulloch, I.; Chueh, C.-C.; Durrant, J. R. Water-Insensitive Electron Transport and Photoactive Layers for Improved Underwater Stability of Organic Photovoltaics. *Adv. Funct. Mater.* **2022**, *32* (40), 2203487.
(14) Zhang, D. F.; Liu, C.; Zhang, K. C.; Jia, Y. H.; Zhong, W. K.; Qiu, W. D.; Li, Y. F.; Heumüller, T.; Forberich, K.; Le Corre, V. M.; Lüer, L.; Li, N.; Huang, F.; Brabec, C. J.; Ying, L. Observation of reversible light degradation in organic photovoltaics induced by long-persistent radicals. *Energy Environ. Sci.* **2023**, *16* (11), 5339−5349.
(15) Zhang, K. N.; Du, X. Y.; Yan, L.; Pu, Y. J.; Tajima, K.; Wang, X. Z.; Hao, X. T. Organic Photovoltaic Stability: Understanding the Role of Engineering Exciton and Charge Carrier Dynamics from Recent Progress. *Small Methods* **2024**, *8* (2), 2300397.
(16) Liu, H. T.; Li, Y. B.; Xu, S. H.; Zhou, Y. H.; Li, Z. A. Emerging Chemistry in Enhancing the Chemical and Photochemical Stabilities of Fused-Ring Electron Acceptors in Organic Solar Cells. *Adv. Funct. Mater.* **2021**, *31* (50), 2106735.
(17) Lee, S.; Jin, J. S.; Moon, H.; Kim, J. H.; Park, K.; Oh, J.; Ki, T.; Jang, S. Y.; Kang, H.; Kim, H.; Lee, K. H. Long-Term Thermal Stability of Nonfullerene Organic Solar Cells via Facile Self-Assembled Interface Passivation. *ACS Energy Lett.* **2023**, *8* (10), 3989−3998.
(18) Ding, P. F.; Yang, D. B.; Yang, S. C.; Ge, Z. Y. Stability of organic solar cells: toward commercial applications. *Chem. Soc. Rev.* **2024**, *53* (5), 2350−2387.
(19) Yan, L. P.; Gu, H. M.; Li, Z. R.; Zhang, J. Q.; Yang, Y. Z.; Wang, H.; Liu, X. G.; Wei, Z. X.; Luo, Q.; Ma, C. Q. The interfacial degradation mechanism of polymer:fullerene bis-adduct solar cells and their stability improvement. *Mater. Adv.* **2020**, *1* (5), 1307−1317.
(20) Liu, B. W.; Su, X.; Lin, Y.; Li, Z. R.; Yan, L. P.; Han, Y. F.; Luo, Q.; Fang, J.; Yang, S. F.; Tan, H. W.; Ma, C. Q. Simultaneously Achieving Highly Efficient and Stable Polymer:Non-Fullerene Solar Cells Enabled By Molecular Structure Optimization and Surface Passivation. *Adv. Sci.* **2022**, *9* (7), 2104588.
(21) Chen, J. X.; Zhang, G. C.; Chen, Z.; Xiao, J. Y.; Xia, T.; Li, X.; Yip, H. L. Fluorescent Conversion Agent Embedded in Zinc Oxide as an Electron-Transporting Layer for High-Performance Non-Fullerene Organic Solar Cells with Improved Photostability. *Small* **2024**, *20* (10), 2306471.
(22) Torto, L.; Rizzo, A.; Cester, A.; Wrachien, N.; Passarini, L.; Krebs, F. C.; Corazza, M.; Gevorgyan, S. A. Analysis of electrical and thermal stress effects on PCBM:P3HT solar cells by photocurrent and impedance spectroscopy modeling. In *2017 IEEE International Reliability Physics Symposium (IRPS)*; IEEE, 2017; pp 2F-4.1−2F-4.10.
(23) Yoon, S.; Schopp, N.; Choi, D. G.; Wakidi, H.; Ding, K.; Ade, H.; Vezin, H.; Reddy, G. N. M.; Nguyen, T. Q. Influences of Metal Electrodes on Stability of Non-Fullerene Acceptor-Based Organic Photovoltaics. *Adv. Funct. Mater.* **2023**, *34* (50), 2308618.
(24) Hermerschmidt, F.; Savva, A.; Georgiou, E.; Tuladhar, S. M.; Durrant, J. R.; McCulloch, I.; Bradley, D. D. C.; Brabec, C. J.; Nelson, J.; Choulis, S. A. Influence of the Hole Transporting Layer on the Thermal Stability of Inverted Organic Photovoltaics Using Accelerated-Heat Lifetime Protocols. *ACS Appl. Mater. Interfaces* **2017**, *9* (16), 14136−14144.
(25) Ding, K.; Li, Y. X.; Forrest, S. R. Characterizing and Improving the Thermal Stability of Organic Photovoltaics Based on Halogen-Rich Non-Fullerene Acceptors. *ACS Appl. Mater. Interfaces* **2022**, *14* (4), 5692−5698.
(26) Lu, Q.; Yang, Z. C.; Meng, X.; Yue, Y. F.; Ahmad, M. A.; Zhang, W. J.; Zhang, S. S.; Zhang, Y. Q.; Liu, Z. H.; Chen, W. A Review on Encapsulation Technology from Organic Light Emitting Diodes to Organic and Perovskite Solar Cells. *Adv. Funct. Mater.* **2021**, *31* (23), 2100151.
(27) Qin, J.; Wu, N.; Chen, W.; Liu, B. W.; Wang, Z. G.; Zhang, L. P.; Yin, N.; Chen, Q.; Zhang, Z. B.; Ma, C. Q. In Situ Solution-Processed Submicron Thick SiO_xC_y/a-SiN_x(O):H Composite Barrier Film for Polymer:Non-Fullerene Photovoltaics. *Small Methods* **2023**, *7* (7), 2300224.
(28) Liu, B.; Han, Y.; Li, Z.; Gu, H.; Yan, L.; Lin, Y.; Luo, Q.; Yang, S.; Ma, C.-Q. Visible Light-Induced Degradation of Inverted Polymer:Nonfullerene Acceptor Solar Cells: Initiated by the Light Absorption of ZnO Layer. *Sol. RRL* **2021**, *5* (1), 2000638.
(29) Jiang, Y.; Sun, L.; Jiang, F.; Xie, C.; Hu, L.; Dong, X.; Qin, F.; Liu, T.; Hu, L.; Jiang, X.; Zhou, Y. Photocatalytic effect of ZnO on the stability of nonfullerene acceptors and its mitigation by SnO2 for nonfullerene organic solar cells. *Mater. Horiz.* **2019**, *6* (7), 1438−1443.
(30) Li, S. T.; Fu, Q.; Meng, L. X.; Wan, X. J.; Ding, L. M.; Lu, G. Y.; Lu, G. H.; Yao, Z. Y.; Li, C. X.; Chen, Y. S. Achieving over 18% Efficiency Organic Solar Cell Enabled by a ZnO-Based Hybrid Electron Transport Layer with an Operational Lifetime up to 5 Years. *Angew. Chem., Int. Ed.* **2022**, *61* (34), No. e202207397.
(31) Han, Y.; Dong, H.; Pan, W.; Liu, B.; Chen, X.; Huang, R.; Li, Z.; Li, F.; Luo, Q.; Zhang, J.; Wei, Z.; Ma, C.-Q. An Efficiency of 16.46% and a T_{80} Lifetime of Over 4000 h for the PM6:Y6 Inverted Organic Solar Cells Enabled by Surface Acid Treatment of the Zinc Oxide Electron Transporting Layer. *ACS Appl. Mater. Interfaces* **2021**, *13* (15), 17869−17881.
(32) Liu, B.-W.; Li, Z.-R.; Yan, L.-P.; Guo, J.-B.; Luo, Q.; Ma, C.-Q. ZnO Surface Passivation with Glucose Enables Simultaneously

Improving Efficiency and Stability of Inverted Polymer: Non-fullerene Solar Cells. *Chin. J. Polym. Sci.* **2022**, *40* (12), 1594−1603.
(33) Qin, Y. P.; Balar, N.; Peng, Z. X.; Gadisa, A.; Angunawela, I.; Bagui, A.; Kashani, S.; Hou, J. H.; Ade, H. The performance-stability conundrum of BTP-based organic solar cells. *Joule* **2021**, *5* (8), 2129−2147.
(34) Sun, C.; Lee, J. W.; Lee, C. Y.; Lee, D. C.; Cho, S. N.; Kwon, S. K.; Kim, B. J.; Kim, Y. H. Dimerized small-molecule acceptors enable efficient and stable organic solar cells. *Joule* **2023**, *7* (2), 416−430.
(35) Ye, L.; Collins, B. A.; Jiao, X. C.; Zhao, J. B.; Yan, H.; Ade, H. Miscibility-Function Relations in Organic Solar Cells: Significance of Optimal Miscibility in Relation to Percolation. *Adv. Energy Mater.* **2018**, *8* (28), 1703058.
(36) Kim, W.; Oh, J.; Park, J.; Sun, Z.; Park, J.; Mai, T. L. H.; Kim, S.; Yang, C. D. Building-up relations between intra- and intermolecular interactions, miscibility, and performance for low-cost, efficient fully non-fused acceptor-based organic solar cells. *Nano Energy* **2023**, *117*, 108853.
(37) Xie, F.; Fang, J.; Zhang, L.; Deng, D.; Chen, Y.; Wei, Z.; Guo, F.; Ma, C.-Q. Correlating the Photovoltaic Performance and Stability of the All-Small-Molecule Organic Solar Cells to Their Intermixed Phases Determined by Concentration-Dependent Ultraviolet-Visible Absorption Spectroscopy. *ACS Appl. Mater. Interfaces* **2024**, *16* (9), 11767−11777.
(38) Doumon, N. Y.; Yang, L. L.; Rosei, F. Ternary organic solar cells: A review of the role of the third element. *Nano Energy* **2022**, *94*, 106915.
(39) de Zerio, A. D.; Müller, C. Glass Forming Acceptor Alloys for Highly Efficient and Thermally Stable Ternary Organic Solar Cells. *Adv. Energy Mater.* **2018**, *8* (28), 1702741.
(40) Hu, L.; Liu, Y.; Mao, L.; Xiong, S. X.; Sun, L. L.; Zhao, N.; Qin, F.; Jiang, Y. Y.; Zhou, Y. H. Chemical reaction between an ITIC electron acceptor and an amine-containing interfacial layer in non-fullerene solar cells. *J. Mater. Chem. A* **2018**, *6* (5), 2273−2278.
(41) Qin, X. X.; Yu, X. L.; Li, Z. R.; Fang, J.; Yan, L. P.; Wu, N.; Nyman, M.; Österbacka, R.; Huang, R.; Li, Z. Y.; Ma, C. Q.; Panunzi, B. Thermal-Induced Performance Decay of the State-of-the-Art Polymer: Non-Fullerene Solar Cells and the Method of Suppression. *Molecules* **2023**, *28* (19), 6856.
(42) Kotadiya, N. B.; Lu, H.; Mondal, A.; Ie, Y.; Andrienko, D.; Blom, P. W. M.; Wetzelaer, G. Universal strategy for Ohmic hole injection into organic semiconductors with high ionization energies. *Nat. Mater.* **2018**, *17* (4), 329−334.
(43) Suo, Z. C.; Liu, J.; Li, S. T.; Yao, Z. Y.; Li, C. X.; Wan, X. J.; Chen, Y. S. An efficient interface modification material for improved efficiency and stability in inverted organic solar cells. *Mater. Chem. Front.* **2024**, *8* (2), 562−566.
(44) Xin, J.; Zhao, C.; Geng, Z.; Xue, W.; Chen, Z.; Song, C.; Yan, H.; Liang, Q.; Miao, Z.; Ma, W.; et al. Elucidate the Thermal Degradation Mechanism of Y6-Based Organic Solar Cells by Establishing Structure-Property Correlation. *Adv. Energy Mater.* **2024**, *14* (30), 2401433.
(45) Greiner, M. T.; Chai, L.; Helander, M. G.; Tang, W. M.; Lu, Z. H. Transition Metal Oxide Work Functions: The Influence of Cation Oxidation State and Oxygen Vacancies. *Adv. Funct. Mater.* **2012**, *22* (21), 4557−4568.
(46) Yin, Y. T.; Pan, X.; Andersson, M. R.; Lewis, D. A.; Andersson, G. G. Mechanism of Organic Solar Cell Performance Degradation upon Thermal Annealing of MoO_x. *ACS Appl. Energy Mater.* **2020**, *3* (1), 366−376.
(47) Nyman, M.; Dahlström, S.; Sandberg, O. J.; Österbacka, R. Unintentional Bulk Doping of Polymer-Fullerene Blends from a Thin Interfacial Layer of MoO3. *Adv. Energy Mater.* **2016**, *6* (15), 1600670.
(48) Sandberg, O. J.; Nyman, M.; Österbacka, R. Direct determination of doping concentration and built-in voltage from extraction current transients. *Org. Electron.* **2014**, *15* (11), 3413−3420.
(49) Nyman, M.; Sandberg, O. J.; Dahlström, S.; Spoltore, D.; Körner, C.; Zhang, Y.; Barlow, S.; Marder, S. R.; Leo, K.; Vandewal, K.; Österbacka, R. Doping-induced carrier profiles in organic semiconductors determined from capacitive extraction-current transients. *Sci. Rep.* **2017**, *7* (1), 5397.
(50) Kirchartz, T.; Gong, W.; Hawks, S. A.; Agostinelli, T.; MacKenzie, R. C. I.; Yang, Y.; Nelson, J. Sensitivity of the Mott−Schottky Analysis in Organic Solar Cells. *J. Phys. Chem. C* **2012**, *116* (14), 7672−7680.
(51) Nyman, M.; Sandberg, O. J.; Li, W.; Zeiske, S.; Kerremans, R.; Meredith, P.; Armin, A. Requirements for Making Thick Junctions of Organic Solar Cells based on Nonfullerene Acceptors. *Sol. RRL* **2021**, *5* (5), 2100018.
(52) Liao, H.-H.; Yang, C.-M.; Liu, C.-C.; Horng, S.-F.; Meng, H.-F.; Shy, J.-T. Dynamics and reversibility of oxygen doping and de-doping for conjugated polymer. *J. Appl. Phys.* **2008**, *103* (10), 104506.
(53) Sandberg, O. J.; Dahlström, S.; Nyman, M.; Wilken, S.; Scheunemann, D.; Österbacka, R. Impact of a Doping-Induced Space-Charge Region on the Collection of Photogenerated Charge Carriers in Thin-Film Solar Cells Based on Low-Mobility Semiconductors. *Phys. Rev. Appl.* **2019**, *12* (3), 034008.
(54) Zeiske, S.; Li, W.; Meredith, P.; Armin, A.; Sandberg, O. J. Light intensity dependence of the photocurrent in organic photovoltaic devices. *Cell Rep. Phys. Sci.* **2022**, *3* (10), 101096.
(55) Schafferhans, J.; Baumann, A.; Wagenpfahl, A.; Deibel, C.; Dyakonov, V. Oxygen doping of P3HT:PCBM blends: Influence on trap states, charge carrier mobility and solar cell performance. *Org. Electron.* **2010**, *11* (10), 1693−1700.
(56) Mihailetchi, V. D.; Koster, L. J. A.; Hummelen, J. C.; Blom, P. W. M. Photocurrent Generation in Polymer-Fullerene Bulk Heterojunctions. *Phys. Rev. Lett.* **2004**, *93* (21), 216601.
(57) Zhu, C.; Tian, J.; Liu, W.; Duan, Y.; Song, Y.; You, Z.; Wang, X.; Li, N.; Zhan, X.; Russell, T. P.; Liu, Y. Batch-Reproducible and Thickness-Insensitive Mesopolymer Zwitterion Interlayers for Organic Solar Cells. *ACS Energy Lett.* **2023**, *8* (6), 2689−2698.
(58) Wöpke, C.; Göhler, C.; Saladina, M.; Du, X.; Nian, L.; Greve, C.; Zhu, C.; Yallum, K. M.; Hofstetter, Y. J.; Becker-Koch, D.; Li, N.; Heumüller, T.; Milekhin, I.; Zahn, D. R. T.; Brabec, C. J.; Banerji, N.; Vaynzof, Y.; Herzig, E. M.; MacKenzie, R. C. I.; Deibel, C. Traps and transport resistance are the next frontiers for stable non-fullerene acceptor solar cells. *Nat. Commun.* **2022**, *13* (1), 3786.

https://doi.org/10.1021/acsami.4c21773
ACS Appl. Mater. Interfaces 2025, 17, 15456−15467